

Chemical Abundances in Active Galaxies

Sophia R. Flury¹^{*} and Edward C. Moran²

¹*Department of Astronomy, University of Massachusetts Amherst, Amherst, MA 01002, United States*

²*Department of Astronomy, Wesleyan University, Middletown, CT 06459, United States*

Accepted 2020 May 29. Received 2020 May 20; in original form 2019 November 12

ABSTRACT

The Sloan Digital Sky Survey (SDSS) has proved to be a powerful resource for understanding the physical properties and chemical composition of star-forming galaxies in the local universe. The SDSS population of active galactic nuclei (AGN) remains as of yet less explored in this capacity. To extend the rigorous study of H II regions in the SDSS to AGN, we adapt methods for computing direct-method chemical abundances for application to the narrow-line regions (NLR) of AGN. By accounting for triply-ionized oxygen, we are able to more completely estimate the total oxygen abundance. We find a strong correlation between electron temperature and oxygen abundance due to collisional cooling by metals. Furthermore, we find that nitrogen and oxygen abundances in AGN are strongly correlated. From the metal-temperature relation and the coupling of nitrogen and oxygen abundances, we develop a new, empirically and physically motivated method for determining chemical abundances from the strong emission lines commonly employed in flux-ratio diagnostic diagrams (BPT diagrams). Our approach, which for AGN reduces to a single equation based on the BPT line ratios, consistently recovers direct-method abundances over a 1.5 dex range in oxygen abundance with an rms uncertainty of 0.18 dex. We have determined metallicities for thousands of AGN in the SDSS, and in the process have discovered an ionization-related discriminator for Seyfert and LINER galaxies.

Key words: ISM: abundances – galaxies: abundances – galaxies: active

1 INTRODUCTION

Spurred by revolutionary ideas about the nature of gaseous nebulae (e.g., [Strömgren 1939](#)), Menzel applied then-new ideas about quantum mechanics to emission-line phenomena to develop a working theory of nebular astrophysics, often in collaboration with Baker and Aller. This enabled the first empirical estimates of physical properties like electron temperature ([Menzel & Aller 1941](#)) and ionic abundances like O⁺/H ([Menzel et al. 1941](#)) in gaseous nebulae. Seyfert, their contemporary, reported the discovery of a new class of emission-line objects in 1943 that later came to be known as active galactic nuclei (AGN). While Menzel’s theory, amended and expanded by astronomers over the following decade or so, has grown commonplace in the research of H II regions, there has been comparatively little application to AGN, preventing the sort of large population studies enjoyed by their line-emitting cousins.

This disparity is perhaps understandable for two reasons: (i) H II regions far outnumber AGN, and many are easily studied due to their location within the Milky Way

and other Local Group galaxies; and (ii) AGN nebulae have a more complex ionization structure (e.g., [Osterbrock & Ferland 2006](#), henceforth OF06). Sixteen years passed between the development of a method for the direct estimation of chemical abundances in the Orion Nebula ([Aller & Liller 1959](#)) and the first investigation of metallicity in an AGN ([Osterbrock & Miller 1975](#)). While [Koski \(1978\)](#) and [Shuder & Osterbrock \(1981\)](#) analyzed the physical properties of the gas in Seyfert nebulae, and [Storchi-Bergmann & Pastoriza \(1990\)](#) established the range of metallicities for a sample of AGN using photoionization models, it was not until [Cruz-Gonzalez et al. \(1991\)](#) that direct-method abundances (i.e., abundances determined using the electron temperature and multi-level atomic models) were computed for a population of Seyferts, a full 50 years after the introduction of the technique.

Because the ionization structure of AGN is complex and highly ionized species are present, high-quality observations and a detailed physical picture of photoionized nebulae in AGN are required for accurate estimates of their elemental abundances. As a possible workaround, it has been demonstrated that the metallicities of the narrow-line regions (NLRs) of Seyfert nuclei can be inferred from the

* E-mail: sflury@umass.edu (SRF)

chemical abundances of nuclear starbursts within the same host galaxies (e.g., [Evans & Dopita 1987](#); [Storchi-Bergmann et al. 1998](#)). Similarly, AGN abundances appear to correlate with radial metallicity gradients observed in the extranuclear H II regions of some Seyfert galaxies ([Dors et al. 2015](#)). However, not all AGN host galaxies have nuclear or extranuclear star-forming regions from which nuclear metallicities can be gleaned — indeed, many are gas-poor “red-and-dead” objects such as bulge-dominated lenticular galaxies. Furthermore, the weakness of the temperature-sensitive [O III] $\lambda 4363$ auroral line can impede efforts to constrain the electron temperature and, therefore, direct-method abundances.

To circumvent these obstacles, astronomers have turned to radiative transfer codes to model the physical and chemical properties of nebulae based on observed emission-line fluxes. This method takes one of several possible forms. The first involves assembling a large set of AGN photoionization models to establish trends between metallicity and line flux ratios so that abundances can be inferred from readily observable emission lines (the “strong” emission lines, or SELs) for an arbitrary AGN sample (e.g., [Storchi-Bergmann et al. 1998](#); [Groves et al. 2004](#); [Pérez-Montero et al. 2019](#)). The second approach requires detailed photoionization modeling of individual AGN, such as the NLR in the Circinus galaxy ([Oliva et al. 1998](#)) or the literature sample of [Dors et al. \(2017\)](#). This approach allows a number of parameters to be varied, including the abundances of individual elements, in order to best predict the observed SEL fluxes. However, while robust in treating the relevant physics, radiative transfer codes such as CLOUDY ([Ferland et al. 2013, 2017](#)) and MAPPINGS ([Sutherland et al. 2013](#); [Sutherland & Dopita 2017](#)) rely on a significant number of assumptions about the nebular environment. Unfortunately, the uncertainties associated with some of the necessary atomic data are substantial, which can introduce systematic error into the emission-line flux predictions. Likewise, information about the shape of the ionizing continuum, the geometry and thermodynamic structure of the nebula, the properties of the dust present, and the equilibrium conditions are required, all of which can influence the predicted strong-line fluxes. Such information is frequently unavailable from observations and must, therefore, be assumed in order to obtain chemical abundances by this approach.

The goal of this study is to develop a robust technique for determining direct-method chemical abundances based on the strong, commonly available emission lines that are measured in large spectroscopic surveys. A reliable direct metallicity method will allow statistically rigorous investigations of the physical and chemical environments of AGN, which ultimately will provide more general insight into the enrichment histories of galactic nuclei. We begin by defining samples of AGN and star-forming galaxies appropriate for such work in § 2. In § 3, we present the physical characteristics of the objects in these samples, which, in conjunction with a multiple ionization-zone model, are used in § 4 to estimate total relative chemical abundances. From these results, we then investigate the effect of cooling by metals on the electron temperature in § 5.1 and the scaling of nitrogen with oxygen in § 5.2. In § 6, we present a simple model for common strong emission line flux ratios from which we develop a new technique for determining chemical abundances in AGN. We verify this method with a compar-

ison between our new method and the direct-method abundances. We then apply this technique to a large sample of AGN and discuss the implications.

2 SAMPLE DEFINITION

In order to perform population analyses of any import, we need a sample of galaxies whose nuclear activity is reliably classified according to “BPT” emission-line flux-ratio diagrams ([Baldwin et al. 1981](#); [Veilleux & Osterbrock 1987](#)). Therefore, we must select objects for which the emission lines necessary for nebular diagnostics are detected in the optical spectrum.

To begin, we employ published emission-line fluxes of galaxies from the Portsmouth processing ([Thomas et al. 2013](#)) of the eighth data release (DR8) of the Sloan Digital Sky Survey (SDSS; [Aihara et al. 2011](#)). In their spectral analysis, the starlight continuum was modeled using penalized pixel fitting (PPXF; [Cappellari & Emsellem 2004](#)) as implemented by the GANDALF code ([Sarzi et al. 2006](#)) with [Maraston & Strömbäck \(2011\)](#) synthetic stellar population (ssp) templates and the [Calzetti \(2001\)](#) extinction law. Emission lines were simultaneously fitted with Gaussian profiles to obtain their fluxes (which we corrected for reddening following the method described in Appendix A). Using these measurements, we have defined a sample of DR8 objects that enable us to investigate the chemical abundances in AGN.

2.1 Parent Samples

Our parent sample is based on the detection of six prominent SELs: H β $\lambda 4861$, [O III] $\lambda 5007$, H α $\lambda 6563$, [N II] $\lambda 6583$, and [S II] $\lambda \lambda 6716, 31$. We require all of these lines to be detected with an amplitude-over-noise (A/N) value of at least 3. This allows us to classify the nuclear activity of the objects using the [N II]/H α vs. [O III]/H β and [S II]/H α vs. [O III]/H β BPT diagnostic diagrams (see Fig. 1). Our classification criteria are as follows. Star-forming galaxies are defined to be objects whose flux ratios fall below and to the left of the empirical curves that demarcate H II and AGN zones on the BPT diagrams ([Kauffmann et al. 2003](#); [Kewley et al. 2006](#)). Objects that are no more than 0.05 dex normal-to-curve over the [Kewley et al. \(2006\)](#) line on the [S II]/H α BPT diagram are also considered to be H II galaxies. AGN are defined to be objects with line ratios that place them above and to the right of the theoretical “maximum starburst” line on the [N II]/H α plot ([Kewley et al. 2001](#)) and at least 0.05 dex above the corresponding demarcation on the [S II]/H α diagram.

For the vast majority of objects, the classifications according to both of the BPT diagnostics are consistent; these make up our “H II” (152,322 objects) and “AGN” (8,720 objects) parent samples.

The redshifts of the galaxies in the parent sample have a maximum value of 0.370 with a median of 0.075. Assuming $H_0 = 73 \text{ km s}^{-1} \text{ Mpc}^{-1}$, the bulk of the objects in the sample lie at distances between 180 Mpc and 420 Mpc.

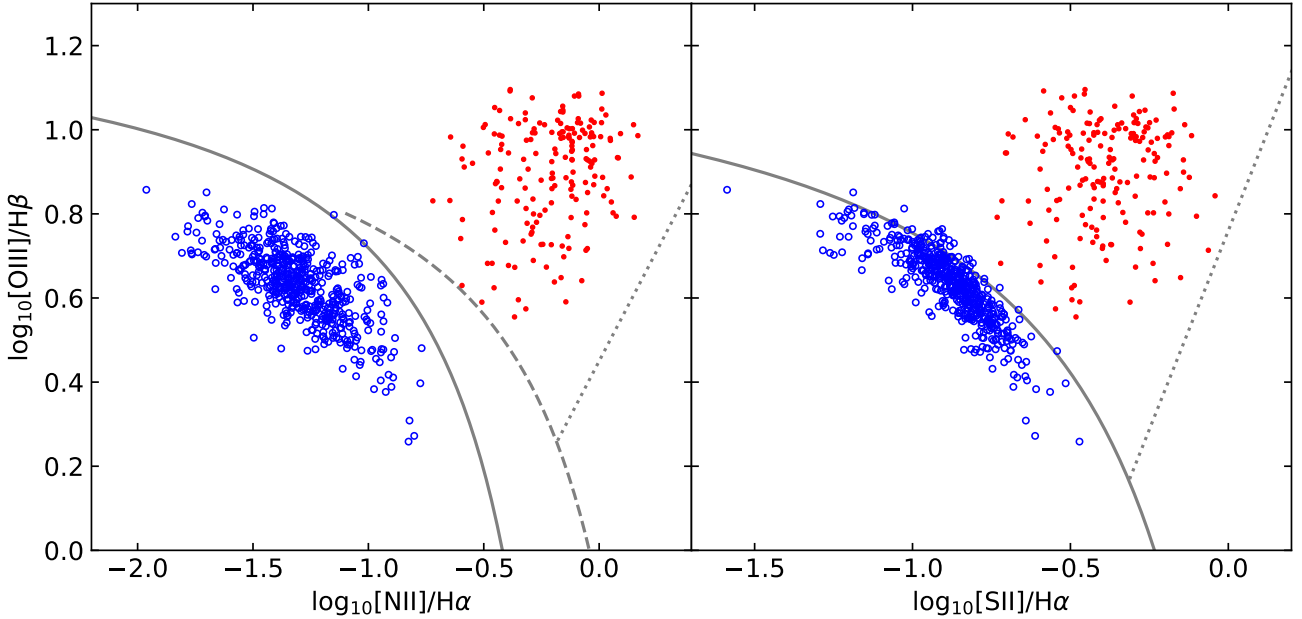


Figure 1. BPT diagnostic diagrams for our samples of AGN (filled red symbols) and H II galaxies (open blue symbols) from the SDSS DR8. The solid curves indicate the empirical demarcations between H II galaxies and AGN defined by Kauffmann et al. (2003) and Kewley et al. (2006). The dashed curve on the [N II]/H α plot represents the theoretical “maximum starburst” line from Kewley et al. (2001). In the AGN zones, empirical divisions between Seyfert galaxies and LINERs (Schawinski et al. 2007; Kewley et al. 2006) are indicated by dotted lines.

2.2 Chemical Abundances Samples

From the parent sample, we culled objects based on criteria for several emission lines to assemble H II and AGN subsamples that can be used to measure chemical abundances. First, we impose a detection of the (weak) [O III] λ 4363 auroral line, which is necessary for the determination of properties such as electron temperature (T_e) and density (n_e) of a photoionized nebula. We further require that $[\text{O III}] \lambda\lambda 4959, 5007 / [\text{O III}] \lambda 4363 > 16$ for the galaxies. This eliminates a small number of objects with improbably high electron temperature estimates ($T_e > 4 \times 10^4$ K for $n_e \sim 10^3 \text{ cm}^{-3}$) due to errors in their reported [O III] λ 4363 fluxes. We also impose the condition that $\sigma_{T_e} / T_e < 1$, where σ_{T_e} is the uncertainty in the derived electron temperature (see § 3). This is to ensure that the values of T_e and n_e we obtain are reasonably well constrained.

We note that these requirements introduce an electron temperature bias for this subset of objects. The relative strength of [O III] λ 4363 increases sharply at $T_e \gtrsim 10^4$ K (e.g., OF06), so the auroral line tends to be more easily detected in high- T_e objects. As discussed by Izotov et al. (2006), a consequence of this bias is that the H II galaxies selected occupy only the “upper” portion of the star-forming locus on BPT diagnostic diagrams (where $[\text{O III}]/\text{H}\beta \gtrsim 2$). This is the lower metallicity portion of the H II distribution, so the correlations we investigate below do not extend to the highest expected metal abundances in star-forming regions.

From the galaxies with detected [O III] λ 4363, we have selected objects with a detected [O II] $\lambda\lambda 3726, 29$ doublet, which is needed to compute oxygen abundances via the di-

rect method. We further limit the sample to those objects for which the derived oxygen abundance (discussed in § 4.2) is fairly well constrained, i.e., $\sigma_{[\text{O}/\text{H}]} < 0.5$ dex. The final H II and AGN samples for abundance measurements contain 539 and 180 galaxies, respectively. Due to the blue wavelength cutoff of ~ 3800 Å in SDSS spectra, all of the objects in these samples have redshifts above $z \approx 0.02$. However, their SEL flux ratios are evenly distributed with respect to those displayed by the parent sample, suggesting that the redshift limit does not bias our abundance investigation in any way.

We note that all objects classified as AGN in this subsample have $[\text{O III}]/\text{H}\beta > 3$ (the traditional threshold for Seyfert galaxies; Veilleux & Osterbrock 1987) and fall in the “Seyfert” zones on BPT diagrams defined by Kewley et al. (2006) and Schawinski et al. (2007). Thus, we can be confident that these objects are powered by accretion onto supermassive black holes.

3 PHYSICAL PROPERTIES

Our assessment of the nebular conditions in the H II and AGN samples employs the five-level atom model for computing the electron density and temperature. For each object, we begin by solving the equilibrium equations for the bound electronic states that correspond to the observed radiative transitions using the open-source software PYNEB (Luridiana et al. 2015), then calculate n_e and T_e iteratively using the measured extinction-corrected [S II] and [O III] line fluxes until the results converge on a consistent set of solutions.

Table 1. Parameters for [S II] doublet ratio vs. electron density for a range of electron temperatures.

T_e (10^4 K)	a_n	b_n (cm^3)	c_n (cm^3)
0.5	1.471	6.710	2.259
1.0	1.450	4.725	1.591
1.5	1.431	3.854	1.298
2.0	1.417	3.326	1.122
2.5	1.406	2.967	1.001
3.0	1.396	2.700	0.909
3.5	1.391	2.483	0.837

3.1 Electron Density

Assuming collisional equilibrium, application of the five-level atom model allows electron density to be computed from the ratio of the fluxes associated with the ${}^2\text{D}_{5/2}^0 \rightarrow {}^4\text{S}_{3/2}^0$ and ${}^2\text{D}_{3/2}^0 \rightarrow {}^4\text{S}_{3/2}^0$ radiative transitions. The [S II] $\lambda\lambda 6716, 31$ and [O II] $\lambda\lambda 3726, 29$ doublets are the common optical emission lines employed to obtain electron density. Because the [O II] doublet is unresolved in the low-resolution SDSS spectra, we derive electron densities using the [S II] doublet. From the equation for collisional equilibrium (see, e.g., Eq. 3.23 in OF06), the ratio of the [S II] doublet emission-line fluxes has the form

$$\frac{j_{\lambda 6716}}{j_{\lambda 6731}} = a_n \frac{1 + b_n n_e}{1 + c_n n_e} \quad (1)$$

where a_n depends on the ratio of collision strengths¹ and b and c depend on the ratio of state population to state de-population rates. Values of these parameters for the relevant range of electron temperatures are listed in Table 1.

We compute the electron density for a given electron temperature by root-finding the value of n_e that minimizes the difference between the observed doublet flux ratio and that predicted by PYNEB. Assuming $T_e = 10^4$ K, this method provides an initial estimate of electron density from the [S II] flux ratio that will need to be recomputed iteratively in tandem with determinations of electron temperature.

3.2 Electron Temperature

For a photoionized gas in collisional equilibrium, the five-level atom model allows electron temperature to be computed from the ratio of the fluxes associated with the ${}^1\text{D}_2 \rightarrow {}^3\text{P}$ and ${}^1\text{S}_0 \rightarrow {}^1\text{D}_2$ radiative transitions. The [O III] $\lambda\lambda 4959, 5007$ doublet and [O III] $\lambda 4363$ auroral line are typically used to derive the electron temperature because [O III] $\lambda 4363$ is often the only diagnostic auroral emission line detected in a spectrum.

As with the electron density, we use PYNEB to compute the [O III] flux ratio for a given T_e and assumed n_e and calculate the temperature which minimizes the difference between the predicted and observed flux ratio. For reference, we express the [O III] temperature diagnostic following Eq. 5.4 in

¹ Following discussion in Ch. 5.6 of OF06, a_n is determined primarily by the ratio of the ${}^2\text{D}^0$ states' statistical weights $g = 2(s + \ell) + 1$. For the [S II] doublet, $a_n \approx 3/2$.

Table 2. Parameters for [O III] doublet-auroral line ratio vs. electron temperature for a range of electron densities.

n_e (cm^{-3})	a_T	$b_T \times 10^4$ K	c_T ($\text{K}^{1/2}$)
10	7.995	3.331	8.937
10^2	7.987	3.330	8.844
10^3	7.964	3.330	8.970
10^4	7.995	3.341	14.913

OF06:

$$\frac{j_{\lambda 4959} + j_{\lambda 5007}}{j_{\lambda 4363}} = \frac{a_T \exp(b_T T_e^{-1})}{1 + c_T T_e^{-1/2}} \quad (2)$$

where a_T depends primarily on the ratio of (${}^1\text{D}_2, {}^3\text{P}$) collision strengths and Einstein coefficients for spontaneous radiation to those of (${}^1\text{S}_0, {}^1\text{D}_2$), b_T scales the electron temperature by the energy difference between the ${}^1\text{S}_0$ and ${}^1\text{D}_2$ states to account for collisional excitation to ${}^1\text{S}_0$, and c_T contains a density term to account for collisional de-excitations. Values of these parameters for a range of electron densities are listed in Table 2.

3.3 Temperature-Density Coupling

As suggested by the above discussion, the electron temperature must be known or assumed to determine the electron density, and vice versa. To address this, we have developed an iterative numerical procedure for computing n_e in tandem with T_e , which yields stable values of both quantities that are consistent with the observed emission-line flux ratios. While PYNEB includes a method for simultaneously solving for n_e and T_e for a given set of flux ratios, it does not account for differences in temperature between the [S II]- and [O III]-emitting zones in a nebula. Our approach, while similar, accounts for these temperature differences.

We begin by computing the electron temperature using a bisection routine, which finds the root corresponding to the difference between the observed [O III] $\lambda\lambda 4959, 5007 / \lambda 4363$ flux ratio and that predicted by PYNEB for the low-density limit (where $n_e \rightarrow 0 \text{ cm}^{-3}$). Then, using a second bisection routine, we compute the electron density by finding the root of the difference between the [S II] $\lambda\lambda 6716, 31$ flux ratio and that predicted by PYNEB. For this calculation, the [O III]-based estimate of T_e is used as input, but it must first be scaled to a value appropriate for the zone where O^+ and S^+ ions reside using the semi-empirical relation

$$T_{e,[\text{O II}]} = \left(\frac{6930}{T_{e,[\text{O III}]}} + 2810 \text{ K}^{-1} \right)^{-1} \quad (3)$$

from Pérez-Montero & Díaz (2003). We then re-compute the electron temperature using the revised estimate of the electron density, and so on. Provided the [S II] flux ratio is theoretically permitted (i.e., between ~ 0.4 and ~ 1.5), this procedure always converges on stable solutions, typically within three to five iterations depending on the tolerance. [S II] flux ratios which fall outside the theoretically permitted range occur in 126 H II galaxies and 8 AGN in our sample. For these objects, we assign a density of 100 cm^{-3} following precedent (e.g., van Zee et al. 1998b; Dors et al. 2013) as this value is plausible for either class of objects under investigation.

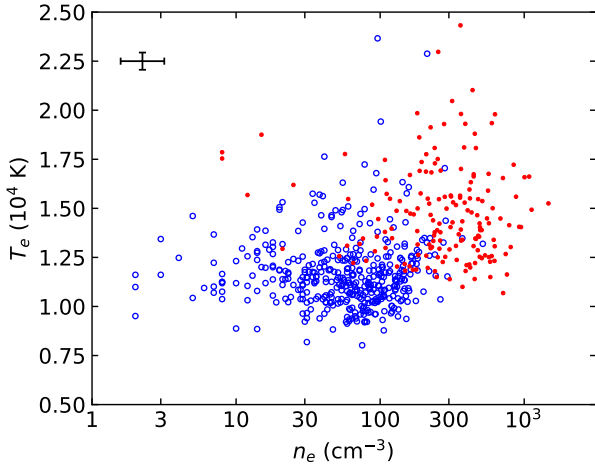


Figure 2. Electron temperatures and densities for the H II galaxies (open blue circles) and AGN (filled red circles) in our sample of SDSS objects. Typical 1σ uncertainties for both quantities are shown in the upper left corner.

Electron temperatures and densities for the galaxies in our sample are plotted in Figure 2. Although temperature and density are formally coupled due to the physics of equilibrium, the two properties are not correlated for either H II galaxies or AGN. However, it is clear that the NLR environments of AGN tend to be hotter and denser than H II regions near the centers of star-forming galaxies. We will return to this point in §5. Excluding objects with [S II] flux ratios that fall outside the theoretical limits, the median density and temperature (with associated dispersions) for the H II galaxies are $\log(n_e/\text{cm}^{-3}) = 1.924 \pm 0.399$ and $T_e = (1.15 \pm 0.23) \times 10^4$ K. For AGN, we find $\log(n_e/\text{cm}^{-3}) = 2.456 \pm 0.382$ and $T_e = (1.43 \pm 0.34) \times 10^4$ K.

4 GAS PHASE ABUNDANCES

To compute gas phase abundances, we employ the direct method using the electron temperatures and densities determined above. For a complete estimate of the relative oxygen abundance, we adopt a three-ionization-zone approximation for nebulae in which oxygen exists in singly, doubly, and triply ionized species. We measure ionic abundances for singly and doubly ionized oxygen and account for triply ionized oxygen with an ionization correction factor. Finally, we validate our approach by comparing our results against those reported for a literature sample of AGN.

4.1 Justification for the Three-Zone Model

The relative amount of O^{+3} in H II regions is usually negligible (e.g., Peimbert & Costero 1969; Kobulnicky et al. 1999; Kennicutt et al. 2003) except in extreme starbursts with a sizable Wolf-Rayet population (e.g., Izotov et al. 2006). However, studies of planetary nebulae, which have harder ionizing spectra than OB associations, have found that O^{+3} , while not the most abundant species of the element, consists

of a non-negligible fraction of the total oxygen with an upper estimate of 20% in extreme cases (e.g., Burgess & Seaton 1960; Rubin et al. 1997).

This must certainly be the case in a Seyfert NLR: the ionizing continuum produced by the central engine possesses significantly more energy per photon than that emitted by OB associations. Indeed, several studies of the [O IV] $\lambda 25.89\mu\text{m}$ mid-infrared emission line have found the line to be far stronger in AGN (particularly Seyferts) than in starburst nuclei (Diamond-Stanic & Rieke 2012; Fernández-Ontiveros et al. 2016) and that the luminosity of [O IV] correlates strongly with X-ray and infrared luminosities (García-Bernete et al. 2016). Given the significance of the [O IV] line in AGN, it stands to reason that the summed ionic abundances must account for O^{+3} in order to appropriately estimate the total oxygen abundance in AGN. Because of the extended partially-ionized zones in AGN, as much oxygen might be contained in the O^0 as in O^{+3} zone. However, hydrogen and neutral oxygen have very similar ionization potentials (13.598 eV and 13.618 eV, respectively). These neutral species are further coupled through charge-exchange reactions, meaning that

$$\frac{\text{O}}{\text{H}} = \left(\frac{\text{O}^0}{\text{H}^0} \right) \quad (4)$$

is necessarily true (cf. Peimbert & Costero 1969; Kobulnicky et al. 1999). However, as there is no means to estimate H^0 from an optical spectrum alone, measurements of the [OI] $\lambda 6300$ flux cannot be used to infer the chemical abundance. As such, only the ionized oxygen is included in estimates of the oxygen abundance relative to H^+ . This gives a final relation for the total relative oxygen abundances of

$$\frac{\text{O}}{\text{H}} = \frac{\text{O}^+ + \text{O}^{+2} + \text{O}^{+3}}{\text{H}^+}. \quad (5)$$

With this established, the remaining work in determining the total oxygen abundance lies in deriving values for the O^+ , O^{+2} , and H^+ ionic abundances and, subsequently, inferring that of O^{+3} with an ionization correction factor (ICF).

4.2 Direct Method Ionic Abundances

While some studies find discrepancies between the direct method for computing abundances from collisionally excited lines (CELs) and recombination lines (e.g., Esteban et al. 2009; Toribio San Cipriano et al. 2017) and photoionization models (e.g., Kewley & Ellison 2008; Dors et al. 2015), an appropriate treatment of ionization structure can account for at least some of the disagreement in the case of Seyferts. Photoionization models rely on assumptions about, among other things, the shape of the ionizing spectrum, dust depletion rates, boundary conditions, and initial conditions, and are also error prone in cases where photoionization cross-sections and collisional strengths are uncertain. Recombination lines are less sensitive to temperature and thermal inhomogeneities than CELs but require exceptionally high SNR spectroscopy to be measured with any confidence.

The direct method of determining abundances from CELs relies on the emissivity

$$j_\lambda = n_{\chi^i} n_e \epsilon_\lambda(n_e, T_e) \frac{4\pi\lambda}{hc}, \quad (6)$$

where $n_{\chi i}$ is the abundance of a particular element χ in ionized species i , and ε_{λ} is the emission coefficient (Eq. 5.41 in OF06). We compute emission coefficient ε_{λ} using PYNEB, which follows Equation 3.20 in OF06. For recombination emission lines, the assumed relationship from Equation 4.14 in OF06 is

$$j_{\lambda} = n_{\chi i} n_e \alpha_{eff} \frac{4\pi\lambda}{hc} \quad (7)$$

where α_{eff} is the effective recombination rate. This effective rate accounts for collisions in the transitional cascade, which populates the state wherefrom an electronic transition occurs to produce a photon at wavelength λ . We use PYNEB to compute the Case B recombination emissivities for hydrogen.

Together with the physical properties estimated in § 3, we compute ε_{λ} for the [O III] $\lambda\lambda 4959, 5007$ doublet and α_{eff} for H β to determine the relative abundance of doubly ionized oxygen, such that

$$\frac{\text{O}^{+2}}{\text{H}^{+}} = \frac{(j_{4959} + j_{5007})\alpha_{4861}}{(\varepsilon_{4959} + \varepsilon_{5007})j_{4861}}. \quad (8)$$

Because we lack measurements of the auroral [O II] lines, we again use the semi-empirical relation from Pérez-Montero & Díaz (2003) to estimate the [O II] electron temperature and compute the emission coefficients for the [O II] $\lambda\lambda 3726, 29$ doublet (see Equation 3 above). This allows us to determine the relative abundance of singly ionized oxygen:

$$\frac{\text{O}^{+}}{\text{H}^{+}} = \frac{(j_{3726} + j_{3729})\alpha_{4861}}{(\varepsilon_{3726} + \varepsilon_{3729})j_{4861}}. \quad (9)$$

Combined, these two ionic abundances give an initial lower limit to the total oxygen abundance but will need to be corrected to account for more highly ionized species.

We also compute the nitrogen abundance relative to oxygen using N $^{+}$ and O $^{+}$ ions. The N $^{+}$ and O $^{+}$ ions occupy similar ionization zones in a photoionized nebula, as indicated by the similarities in both neutral and singly-ionized species' ionization potentials, allowing these to be used as a proxy for the nitrogen abundance relative to oxygen (e.g. Peimbert & Costero 1969). We proceed with the assumption that N/O = N $^{+}$ /O $^{+}$ (Peimbert 1968; Peimbert & Costero 1969). From Equation 18 in Peimbert (1968), we obtain

$$\frac{\text{N}}{\text{H}} = \frac{\text{N}}{\text{O}} \times \frac{\text{O}}{\text{H}}. \quad (10)$$

As was done with the relative oxygen abundances, we compute collisional emission coefficients using PYNEB to determine the relative ionic abundance ratio

$$\frac{\text{N}^{+}}{\text{O}^{+}} = \frac{(j_{6548} + j_{6583})(\varepsilon_{3726} + \varepsilon_{3729})}{(j_{3726} + j_{3729})(\varepsilon_{6548} + \varepsilon_{6583})}. \quad (11)$$

Because the low ionization zones for the two elements largely occupy the same region of the nebula, we assume when computing the emissivities that the electron temperature for singly-ionized nitrogen is the same as that of singly-ionized oxygen.

4.3 Ionization Correction Factor

It is necessary, especially in the case of AGN, to account for oxygen locked up in unobserved ionic species like O $^{+3}$ using an ICF. The similarity between the O $^{+2}$ and He $^{+}$ ionization

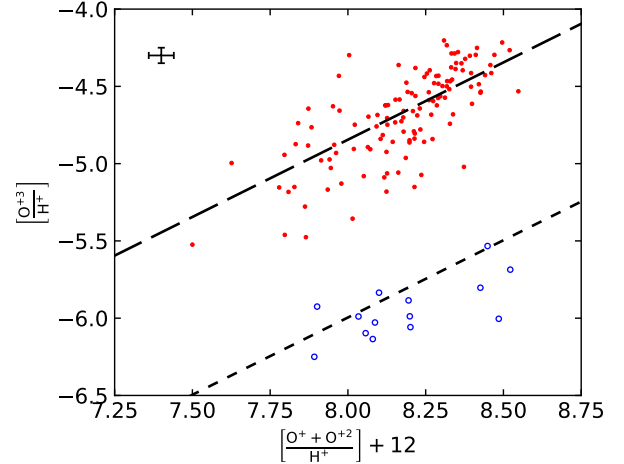


Figure 3. The [O $^{+3}$ /H $^{+}$] abundance as a function of two-zone oxygen abundances for objects in our sample for which the fluxes of He 1 $\lambda 5875$ and He 2 $\lambda 4686$ are measured. The short-dashed line represents 1% of the oxygen locked up in the triply ionized species, while the long-dashed line represents 12.5%. Symbols are the same as in Figure 1.

potentials (54.936 eV and 54.417 eV, respectively) allows one to write

$$\frac{\text{O}^{+3}}{\text{O}^{+} + \text{O}^{+2} + \text{O}^{+3}} \propto \frac{\text{He}^{+2}}{\text{He}^{+} + \text{He}^{+2}} \quad (12)$$

in order to infer the abundance of O $^{+3}$. Because He 0 ionizes at 24.59 eV while O 0 ionizes at 13.62 eV, a proportionality factor p_{ICF} is necessary to complete the relation by accounting for the difference in ionization structure for the two elements. O $^{+}$ and O $^{+2}$ have an average ionization potential of 24.369 eV, which is close to that of neutral helium. It stands to reason, then, that taking the mean of the O $^{+}$ and O $^{+2}$ abundances can correct for the mismatch in the O and He ionization zones. This gives $p_{\text{ICF}} = 0.5$, as suggested by Izotov et al. (2006), resulting in a final ICF of

$$\text{O}^{+3} = 0.5 \frac{y}{1-y} (\text{O}^{+} + \text{O}^{+2}), \quad (13)$$

where $y = \text{He}^{+2}(\text{He}^{+} + \text{He}^{+2})^{-1}$.

We apply this ICF to all objects in our sample for which He 1 $\lambda 5875$ and He 2 $\lambda 4686$ fluxes have been measured (with A/N > 2) by the Portsmouth group. This comprises 125 AGN and 13 H II galaxies. For these objects, the [O $^{+3}$ /H $^{+}$] ionic abundances estimated by this method are shown in Figure 3. As the Figure indicates, there is a clear difference in the typical [O $^{+3}$ /H $^{+}$] values for Seyfert and star-forming galaxies. For the AGN, ~ 12.5% of the total ionic oxygen abundance exists in the O $^{+3}$ /H, while for H II galaxies the percentage is ~ 1% at best.

For galaxies lacking helium line fluxes, we use the fractional O $^{+3}$ implied by the typical ICF measured for objects of the same activity class, and estimate He $^{+}$ and He $^{+2}$ using the He 1 and He 2 Case B recombination coefficients computed by PYNEB with the O $^{+2}$ electron temperatures. With values of [O $^{+3}$ /H $^{+}$] for all objects in our sample, we now have abundances for each species necessary to solve for the

oxygen abundance relative to hydrogen using Equation 5. We compute O/H for each object and express the results following standard convention: $[\text{O}/\text{H}]+12 = \log_{10}(\text{O}/\text{H}) + 12$. We find that the H II galaxies in our sample have a median $[\text{O}/\text{H}]+12$ of 8.197 with an rms of 0.166 dex, while the Seyferts have a median $[\text{O}/\text{H}]+12$ of 8.230 with an rms of 0.249 dex. Propagating the errors in the emission-line fluxes through the calculations, we have obtained the uncertainty in the direct-method abundance for each object in our sample. Typical uncertainties of 0.040 dex for $[\text{O}/\text{H}]+12$ and 0.054 dex for $[\text{N}/\text{H}]+12$ are found for H II galaxies. Flux errors tend to be larger for the AGN in our SDSS sample, which results to somewhat higher typical uncertainties: 0.095 dex for $[\text{O}/\text{H}]+12$ and 0.132 dex for $[\text{N}/\text{H}]+12$.

4.4 Comparison with the Literature

In a complementary study, Dors et al. (2015) compiled emission-line fluxes (including $[\text{O III}] \lambda 4363$) for 47 local ($z < 0.1$) Seyfert nuclei. Based on these data, they computed electron temperatures and densities and direct-method abundances for all of the objects, which provides an opportunity to validate the abundance method outlined above.

We begin by comparing the electron temperatures and densities reported for the Dors et al. (2015) sample to those obtained for the same objects via our approach (§ 3). This will allow us to isolate any differences in the values assumed for these quantities when we compare abundance determination methods. As Figure 4 demonstrates, the Dors et al. (2015) temperatures and densities are, for the most part, in close agreement with ours. However, substantial differences exist for $\sim 20\%$ of the sample: there are four objects for which the derived electron densities disagree by at least a factor of two, and five objects for which the electron temperatures disagree by more than 10^3 K. The discrepancies stem from a difference in the method used to calculate these values. Although the TEMDEN routine they used computes n_e iteratively (accounting for electron temperature), the method they employed to estimate T_e does not simultaneously account for electron density. Moreover, the TEMDEN routine does not account for the difference in T_e between the O^{+2} and O^{+} zones when calculating n_e .

There are a few differences between the method for determining abundances described in § 4.2 and that presented by Dors et al. (2015). The first concerns the inclusion of a correction for triply ionized oxygen. As demonstrated in Figure 3, a considerable fraction of oxygen in AGN exists in the O^{+3} state and cannot be ignored. We therefore corrected the abundances reported by Dors et al. (2015) assuming that 12.5% of oxygen exists in the O^{+3} state prior to comparing them to the values we obtain for their sample. Additional differences include the approach and atomic data used to compute emissivities. However, as Figure 5 shows, these differences are not very significant. The median offset between the O^{+3} -corrected Dors et al. (2015) abundances and those we calculate is only ~ 0.11 dex. If we replace the Dors et al. (2015) electron temperatures with those derived using the approach outlined in § 3, the median offset drops to 0.05 dex. We note that the discrepancy between the abundance measurements increases as $[\text{O}/\text{H}]+12$ decreases, which could be due to increases in electron temperature (see § 5.1). But overall, the agreement between the Dors et al. (2015)

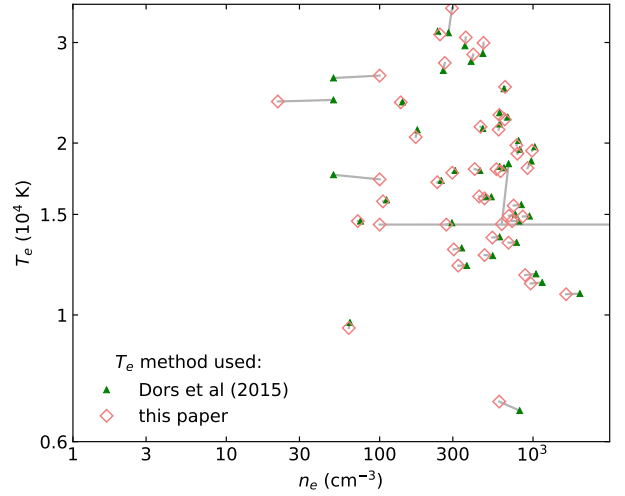


Figure 4. Comparison of electron temperatures and densities for the Dors et al. (2015) AGN sample computed using their method (filled green triangles) and the one outlined in § 3 of this paper (open red diamonds).

abundances and ours is excellent, indicating that the direct method developed here can be employed with confidence.

5 SEMI-EMPIRICAL RELATIONS

5.1 Cooling Sequences

Metals have long been known to act as an important source of cooling in gaseous nebulae (Spitzer 1949), and there is observational support (Kobulnicky et al. 1999) for the theoretically expected relationship between electron temperature and chemical abundance (e.g., McGaugh 1991; López-Sánchez et al. 2012). However, a comprehensive picture of the cooling process has yet to emerge. For example, Kobulnicky et al. (1999) found a strong correlation between T_e and metallicity using a sample of 69 extragalactic H II regions (see their Fig. 5), but did not provide a physical description of the relationship. Conversely, López-Sánchez et al. (2012) derived a cooling sequence (i.e., the relation between temperature and metal coolants demonstrated by the T_e vs $[\text{O}/\text{H}]$ diagram) for model H II regions over the full range of typical metallicities, but did not compare their results to observations. More recently, Nicholls et al. (2014) have provided a mathematical description of the cooling sequence for a large sample of extragalactic H II regions and a comparison between the data and predictions of photoionization models to shed light on the physical mechanisms related to cooling. However, their results are only applicable to low-metallicity objects, i.e., those with $[\text{O}/\text{H}]+12 < 8.4$. Here, we extend the characterization of cooling process to star-forming regions with $[\text{O}/\text{H}]+12 \approx 9$.

To investigate nebular cooling over the broadest possible range of temperatures and metallicities, we have supplemented our SDSS sample with data from the literature: 47 Seyferts with direct-method abundances from Dors et al. (2015) and 414 extragalactic H II regions from Pilyugin et al.

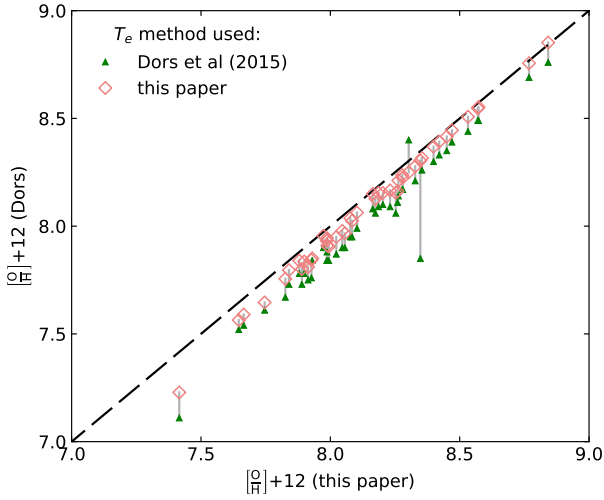


Figure 5. Direct-method oxygen abundances of AGN computed by Dors et al. (2015) compared to those calculated for the same objects using the direct method developed in this paper. Based on the results presented in Figure 3, the abundances published by Dors et al. (2015) have been corrected for O^{+3} assuming this species represents 12.5% of the total oxygen (filled green triangles). Additionally, we show the values yielded by the Dors et al. (2015) method if the approach described in § 3 for estimating electron temperatures is employed (open red diamonds). Clearly, there is close agreement between these abundances and those derived using our method.

Table 3. Cooling sequence coefficients.

	$x = [O/H] + 12$		$x = \log_{10} t_4$	
	H II	AGN	H II	AGN
a_0	-0.143	-0.050	-1.302	-1.948
a_1	3.171	1.372	-2.917	4.108
a_2	-23.551	-12.792	-2.500	-4.175
a_3	58.937	40.290	8.304	8.803

(2012). After correcting the Pilyugin et al. (2012) and Dors et al. (2015) abundances for $[O^{+3}/H^+]$, we fitted the cooling sequences for H II regions and AGN with a third-order polynomial of the form

$$y = a_3x^3 + a_2x^2 + a_1x + a_0 \quad (14)$$

where $x = [O/H] + 12$ and $y = \log_{10} t_4$ (again, $t_4 = T_e/10^4$ K). The results are displayed in Figure 6, and the corresponding coefficients for each semi-empirical sequence are listed in Table 3. The Table also includes the coefficients obtained for fits where $x = \log_{10} t_4$ and $y = [O/H]$, for the purpose of inferring $[O/H]$ from T_e .

Figure 6 represents the first empirical cooling sequence for Seyfert galaxies. Ostensibly, the same cooling mechanisms are at play in both AGN and H II galaxies: collisions, recombination, and free-free interactions dissipate the kinetic energy of the electron gas in the form of electromagnetic radiation. However, the AGN sequence is characterized by higher temperatures, and it lacks the dramatic drop in T_e seen in H II regions with higher metallicities. This is likely

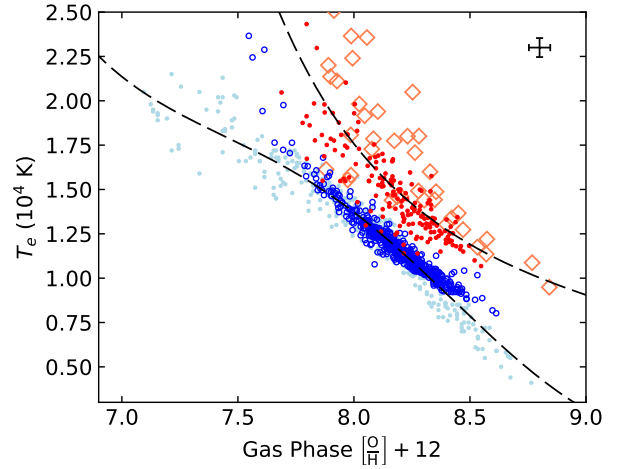


Figure 6. Electron temperature vs. oxygen abundance for AGN and star-forming galaxies included in several different studies. Open blue and filled red circles represent H II galaxies and AGN, respectively, from our SDSS sample with median $1 - \sigma$ uncertainties shown in the upper right. Light blue circles represent extragalactic H II regions from Pilyugin et al. (2012), and the locations of the Dors et al. (2015) AGN are indicated with open red diamonds. We have corrected metallicities reported by Pilyugin et al. (2012) and Dors et al. (2015) to account for the O^{+3} species.

to be a consequence of the fact that AGN impart more kinetic energy per electron during the photoionization process than O and B stars do. The initially higher electron velocities reduce the rate of recombination in AGNs², which is a significant source of cooling in the O^{+2} region by means of the $He^+ + e^- \rightarrow He^0 + \gamma$ process. Thus, the gas is prevented from dissipating the increased thermal energy (OF06; Groves et al. 2004).

In addition to providing insight into nebular heating rates, the cooling sequences shown in Figure 6 have practical applications. When t_4 is treated as the independent variable, one can infer the direct-method metallicity using T_e if measurements of the $[O II]$ doublet and/or ICF helium recombination lines are not available. Similarly, if measurements of the $[O III]$ auroral line are lacking, one could estimate the oxygen abundance by computing SEL emission coefficients for different values of $[O/H]$ and the corresponding electron temperature indicated by the cooling sequence to recover the observed flux ratios. However, such an approach would require additional information, such as the production rate of other elements relative to oxygen.

5.2 Nitrogen Production

Variations in H II region emission line flux ratios have been observed in spiral galaxies as early as the 1940s (c.f., Aller 1942). The Searle (1971) survey of extragalactic H II regions

² As discussed in Ch. 5.11 of OF06, recombination rates are approximately proportional to the inverse of the electron temperature, due in part to the preferential recombination of electrons with low velocities.

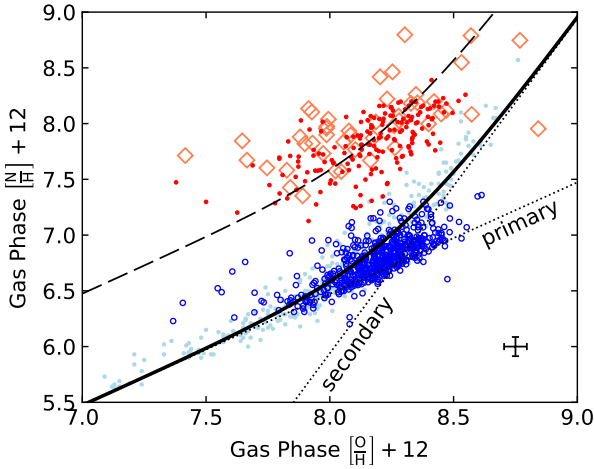


Figure 7. Nitrogen abundance vs. oxygen abundance for AGN and star-forming galaxies included in several different studies. Symbols as in Figure 6. The solid line represents our fit to the H II nitrogen production sequence. Dotted lines represent the primary and secondary nitrogen components of the relation. The dashed lines represents the H II nitrogen production relation shifted by 0.75 dex in $[N/H]$ and 0.125 in $[O/H]$ to match the observed AGN abundances.

in the arms of four spiral galaxies demonstrated radial gradients in $[O\text{ III}]/H\beta$ and $[N\text{ II}]/H\alpha$ and provided an explanation for the phenomenon: radial gradients in the oxygen and nitrogen abundances relative to hydrogen. Initial efforts to explore the Searle (1971) suggestion that nitrogen abundances scale with those of oxygen assumed that nitrogen is solely a secondary element (e.g. Talbot & Arnett 1974), meaning the predicted nitrogen abundances depend entirely on the initial stellar carbon abundances. Alloin et al. (1979) introduced the first physically complete model of the co-evolution of nitrogen and oxygen. In their scheme, both primary nitrogen (i.e., dependent on carbon formed in situ by helium burning) and secondary nitrogen are significant. The Alloin et al. (1979) predictions provided an accurate description of the $[N/H]$ - $[O/H]$ correlation observed at that time. Based on this framework, Vila-Costas & Edmunds (1993) modeled a much larger sample of H II region nitrogen abundances relative to oxygen. Together with the subsequent van Zee et al. (1998b) study of 185 H II regions in 13 galaxies, this provided substantial evidence in support of the combined primary-secondary nitrogen production hypothesis.

To demonstrate the nitrogen-oxygen coupling for both H II galaxies and AGN, we compare the $[N/H]+12$ and $[O/H]+12$ results from both our subsample and those from the literature in Figure 7. We assume that the primary and secondary nitrogen each follow a log-linear relation (e.g., Vila-Costas & Edmunds 1993; Groves et al. 2004; Gutkin et al. 2016; Nicholls et al. 2017) and fit the H II galaxies with the sum of the two relations to obtain

$$\frac{N}{H} = \frac{O}{H} \left(10^{-1.527} + 10^{2[O/H]+5.940} \right). \quad (15)$$

This fit is shown in Figure 7 along with the individual primary and secondary nitrogen production components.

As seen in the cooling sequences, Figure 7 shows that

the AGN form a unique correlation distinctly offset from that of the H II galaxies. We find the AGN nitrogen abundances are typically 1 dex higher than those in H II galaxies of the same $[O/H]$ values. The shape of the distribution of AGN $[N/H]$ values suggests the offset is solely in nitrogen abundance. To demonstrate this, we multiply the right side of Equation 15 by a factor of 10 and find reasonable agreement between the adjusted description and the measured AGN abundances.

This is not the first time nitrogen excess has been noted in AGN: Dors et al. (2015) found a separation of as much as 2 dex between direct method $[O/H]$ values and those inferred following Storchi-Bergmann et al. (1998), the latter using the nitrogen-oxygen relation of Vila-Costas & Edmunds (1993). To account for the discrepancy, Dors et al. (2015) propose that this shift in $[O/H]$ is due to temperature fluctuations or shock heating of the NLR gas, either of which would artificially inflate the estimated electron temperature and thus decrease the measured $[O/H]$. It is possible that infall, outflow, and star formation efficiency could collectively inflate the nitrogen abundance (e.g., Vincenzo et al. 2016); however, these processes only account for, at most, a few tenths of a dex in $[N/O]$ and are likely insufficient in explaining the 1 dex difference in nitrogen abundances we measure in AGN.

While significant in demonstrating the evolution of gas phase abundances and possible complications for the direct-method abundances, the $[N/H]$ - $[O/H]$ diagram provides an important basis for understanding the chemical composition of nebulae. For instance, photoionization models rely heavily on the nitrogen-oxygen scaling relations (e.g., Storchi-Bergmann et al. 1998; Groves et al. 2004; Gutkin et al. 2016) to make accurate predictions for flux-ratio diagnostic diagrams like the BPT because, as shown in § 4.2, abundances directly determine emission line fluxes. If one can infer emissivity ratios from the oxygen abundance, such as we have established with the cooling sequences, then Equation 15 provides the tool necessary for predicting $[O\text{ III}]/H\beta$ and $[N\text{ II}]/H\alpha$ BPT flux ratios for a given value of $[O/H]$, enabling the inference of metallicity solely from SELs. We explain and demonstrate this approach in detail the next section and examine the results.

6 A NEW METHOD FOR ABUNDANCE ESTIMATION

Previous approaches to determining relative abundances have relied on either SEL-abundance correlations for H II regions and galaxies (e.g., van Zee et al. 1998a; Pettini & Pagel 2004), which have not been validated for AGN, or radiative transfer models, which require many assumptions about the ionizing source and the physical conditions present in the nebula (e.g., Storchi-Bergmann et al. 1998; Dors et al. 2017). In this section, we present a new method for estimating direct-method oxygen abundances for AGN based solely on the SEL flux ratios that are routinely employed in BPT diagnostic diagrams.

Table 4. BPT emissivity ratio parameters for Equation 18.

$\log_{10}(\varepsilon_{\chi^i}/\varepsilon_{\text{H}^+})$	a_ε	b_ε	c_ε
$[\text{N II}]/\text{H}\alpha$	-1.003	9.800×10^{-2}	5.195
$[\text{O III}]/\text{H}\beta$	-1.381	6.845×10^{-5}	5.845

6.1 A Simple Equilibrium Model

Our SEL approach for estimating abundances involves a reverse-engineering of the direct method outlined above in § 4. We begin by using Equations 6 and 7 to obtain (a) the $[\text{N II}]/\text{H}\alpha$ flux ratio

$$\frac{j_{\lambda 6583}}{j_{\lambda 6563}} = \frac{\text{N}^+}{\text{H}^+} \frac{\varepsilon_{\lambda 6583}(T_e, n_e)}{\alpha_{\lambda 6563}(T_e)} \quad (16)$$

from the relative ionic abundance N^+/H^+ and the $[\text{O II}]$ electron temperature (see § 3.3), and (b) the $[\text{O III}]/\text{H}\beta$ flux ratio

$$\frac{j_{\lambda 5007}}{j_{\lambda 4861}} = \frac{\text{O}^{+2}}{\text{H}^+} \frac{\varepsilon_{\lambda 5007}(T_e, n_e)}{\alpha_{\lambda 4861}(T_e)} \quad (17)$$

from the relative ionic abundance O^{+2}/H^+ and the $[\text{O III}]$ electron temperature. The process of estimating the emissivity ratios in these two equations is simplified by computing each value of ε and α_{eff} with PYNEB assuming a typical electron density of 100 cm^{-3} (see § 3). The ratio of emissivities can then be fitted with the analytic expression

$$\log_{10} \left(\frac{\varepsilon_{\chi^i}}{\varepsilon_{\text{H}^+}} \right) = \frac{a_\varepsilon}{t_4 + b_\varepsilon} + c_\varepsilon, \quad (18)$$

to obtain a relation between emissivity and electron temperature. The coefficients associated with the $[\text{N II}]/\text{H}\alpha$ and $[\text{O III}]/\text{H}\beta$ flux ratios are listed in Table 4.

As we have related electron temperature and metallicity by means of the cooling sequences (§ 5.1), we can eliminate the temperature dependence of Equation 18 by substituting Equation 14 (with the parameters for $x = [\text{O}/\text{H}] + 12$ listed in Table 3) for t_4 . This allows the emissivity ratios for $[\text{N II}]/\text{H}\alpha$ and $[\text{O III}]/\text{H}\beta$ to be computed for a given value of $[\text{O}/\text{H}] + 12$. Furthermore, the $[\text{N}/\text{H}]$ - $[\text{O}/\text{H}]$ coupling established in § 5.2 allows us to express the nitrogen abundance as a function of the oxygen abundance via Equation 15. All that remains to be determined is the fraction of the total abundance associated with each ionic species.

The ionic abundances can be expressed in terms of total abundances to indicate the fraction of a given metal in a particular state of ionization, i.e., the *ion fraction*. For doubly-ionized oxygen, we define the ion fraction η such that

$$\eta = \frac{\text{O}^{+2}}{\text{O}}, \quad (19)$$

which gives

$$\frac{\text{O}^{+2}}{\text{H}^+} = \eta \frac{\text{O}}{\text{H}}. \quad (20)$$

The ion fraction for N^+ can be expressed in terms of η and an addition variable ζ , which accounts for the fraction of oxygen contained in the O^{+3} species, such that, ultimately,

$$\frac{\text{N}^+}{\text{H}^+} = (1 - \eta - \zeta) \frac{\text{N}}{\text{H}}. \quad (21)$$

The ICF computed from helium recombination lines (see Figure 3) establishes the characteristic fraction of oxygen contained in the O^{+3} species for AGN and H II galaxies:

$$\zeta \approx \begin{cases} 0.01 & \text{H II} \\ 0.125 & \text{AGN} \end{cases}. \quad (22)$$

As η relates total abundances to ionic abundances, values of the $[\text{N II}]/\text{H}\alpha$ (Eq. 16) and $[\text{O III}]/\text{H}\beta$ (Eq. 17) flux ratios can be expressed solely in terms of $[\text{O}/\text{H}]$ and η for each type of object:

$$\frac{j_{\lambda 6583}}{j_{\lambda 6563}} = (1 - \eta - \zeta) \frac{\text{N}}{\text{H}} \left(\frac{\text{O}}{\text{H}} \right) \frac{\varepsilon_{\lambda 6583}}{\alpha_{\lambda 6563}}(t_4(\text{O}/\text{H})) \quad (23)$$

and

$$\frac{j_{\lambda 5007}}{j_{\lambda 4861}} = \eta \frac{\text{O}}{\text{H}} \frac{\varepsilon_{\lambda 5007}}{\alpha_{\lambda 4861}}(t_4(\text{O}/\text{H})) \quad (24)$$

Using these equations, we have calculated grids of predicted flux ratios for H II galaxies and AGN over reasonable ranges of ion fraction and oxygen gas phase abundance. These grids are overlaid on the $[\text{O III}]/\text{H}\beta$ vs. $[\text{N II}]/\text{H}\alpha$ diagnostic diagram in Figure 8. It is clear from the figure that our predictions are consistent with the flux ratios observed for both populations.

A close examination of the H II galaxy predictions shown in Figure 8 reveals that, for a fixed value of η , the $[\text{O III}]/\text{H}\beta$ flux ratio increases with $[\text{O}/\text{H}] + 12$ at first, but then declines precipitously at higher metallicities (cf. the photoionization model predictions of constant ionization parameter in Stasińska et al. 2006). The maximum in $[\text{O III}]/\text{H}\beta$ occurs at $[\text{O}/\text{H}] + 12 = 8.124$ for all values of η , which, according to the H II cooling sequence (see Eq. 14 and Table 3) corresponds to a threshold electron temperature of $T_{e, \text{thresh}} = 1.2 \times 10^4$ K. Above this metallicity, the increase in oxygen abundance is offset by a decrease in electron temperature, which results in fewer collisionally excited O^{+2} ions overall and, thus, a decrease in the $[\text{O III}]/\text{H}\beta$ ratio. This behavior causes the grid of predicted line ratios to fold over on itself, in the sense that line ratios for objects with extremely high values of η and $[\text{O}/\text{H}] + 12$ would nearly overlap with those for which both η and $[\text{O}/\text{H}] + 12$ are very low.

The apparent “crease” in the fold roughly follows the locus of observed points for H II galaxies, along which clear trends in η and $[\text{O}/\text{H}] + 12$ are evident. For example, as $\log [\text{O III}]/\text{H}\beta$ increases from -0.75 to 0.0 to $+0.75$, η increases from $\lesssim 0.3$ to $\sim 0.2 - 0.6$ to $\gtrsim 0.75$, and $[\text{O}/\text{H}] + 12$ decreases from $\gtrsim 8.5$ to ~ 8.5 to $\lesssim 8.25$. Following predictions from photoionization models, others have proposed that metallicity is a direct cause for the location and shape of the H II sequence (e.g., Stasińska et al. 2006; Kewley et al. 2013), which is consistent with the trend we see in $[\text{O}/\text{H}] + 12$ in our grid of flux ratios. Assuming that OB stars in H II galaxies and the nebulae they power have similar metallicities, the run of η with $[\text{O}/\text{H}] + 12$ along the star-forming locus can be understood as a consequence of stars’ ionizing radiation decreasing with an increase in metallicity by means of physical processes such as line blanketing, which is consistent with the current understanding of stellar ultraviolet continua (e.g., Levesque et al. 2010; Kewley et al. 2013).

We note that there is scatter in the data used to derive the cooling sequence (Eq. 14) and nitrogen production relation (Eq. 15). Accounting for this scatter would permit a maximum shift in the H II line-ratio grid of about $+0.1$ dex

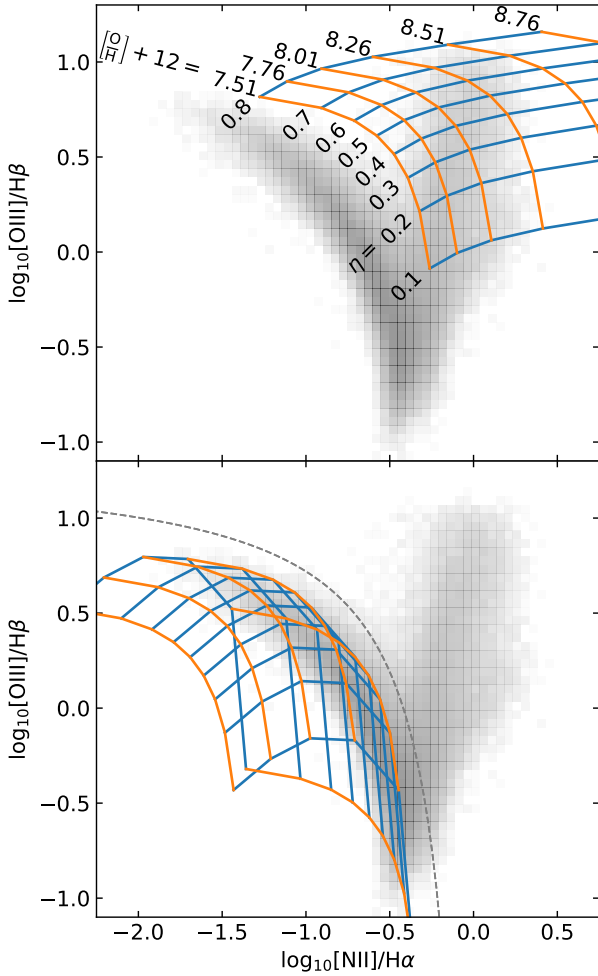


Figure 8. Grids of flux ratio predictions based on our simple equilibrium model for AGN (top) and H II regions (bottom). Shown in grey are line ratios for the objects in our parent SDSS sample. Values of $[O/H]+12$ range from 7.51 to 8.76 in increments of 0.25 dex. Values of η , the O^{+2} ion fraction, range from 0.1 to 0.9 for H II galaxies and from 0.1 to 0.8 for AGN. The short-dashed curve in the lower panel indicates the empirical demarcation between AGN and star-forming galaxies from [Kauffmann et al. \(2003\)](#).

in $[N II]/H\alpha$ and $+0.05$ dex in $[O III]/H\beta$. This shift would place the “crease” in the grid along, but not over, the empirical curve from [Kauffmann et al. \(2003\)](#) that separates H II galaxies and other types of emission-line objects on the BPT diagram. Moreover, the crease in our grid closely matches the upper limit predicted by [Stasińska et al. \(2006\)](#) using photoionization models. This close proximity of our model flux ratios to empirical and theoretical predictions bolsters our confidence in the accuracy of the flux ratio predictions. Given the dependence of the grid’s location on nitrogen abundance and electron temperature, we surmise that the breadth of the H II galaxy locus on the diagram is due in part to small variations in $[N/H]$ and T_e amongst objects with the same value of $[O/H]$.

As Figure 8 indicates, the region of the BPT diagram occupied solely by AGN is largely covered by the grid of

predicted flux ratios. Moreover, at the lowest metallicities considered, our predictions for AGN fall above the [Kauffmann et al. \(2003\)](#) curve. Note that for a fixed value of η , the $[O III]/H\beta$ ratio does not turn over as $[O/H]+12$ increases, so there is no “folding” of the model grid as in the case for H II galaxies. This is due to the fact that $T_{e,thresh}$ occurs at a substantially higher metallicity in the AGN cooling sequence. The decrease in electron temperature with increasing $[O/H]$ results instead in the modest gradient seen in $[O III]/H\beta$. As discussed below, the lack of folding of the AGN grid is quite fortunate: it ensures that pairs of line ratios map uniquely to values of the oxygen abundance.

6.2 Comparison to the Direct Method

To obtain AGN metallicities from our SEL model, we employ Equations 23 and 24 to generate a grid an order of magnitude finer than that shown in Figure 8 and compute the two-dimensional bicubic interpolation of $[O/H]+12$ (and, separately, of η) with respect to the predicted flux ratios. For our sample of SDSS AGN, we have compared abundances estimated this way to those determined via the direct method described in §§ 4.2–4.3. The results, displayed in Figure 9, indicate that the agreement between SEL and direct method abundances is very good. The horizontal error bar in the Figure represents the median uncertainty in the direct-method values of $[O/H]$ (§ 4.3). The width of the grey region on the diagram, which includes 68% of the points, implies that on average an additional error of 0.15 dex (shown by the vertical error bar) is incurred when the SEL method is applied. In total, a typical 1σ uncertainty of ~ 0.18 dex is expected for the SEL abundances. While this may be insufficient for certain applications, our SEL method provides a means to obtain a robust, empirically based metallicity estimate for any AGN classified via the $[O III]/H\beta$ vs. $[N II]/H\alpha$ BPT diagram, which previously has not been possible.

6.3 Extension to the Parent Sample

To illustrate the general utility of our SEL abundance method, we have applied it to the 8,720 AGN in the SDSS parent sample described in § 2.1. Color-coded metallicities for these objects are plotted as a function of their BPT flux ratios in Figure 10. As anticipated from Figure 8, the values of $[O/H]+12$ observed for AGN span more than an order of magnitude. Low-metallicity AGN (with predominantly high values of η) are present, but are rare. This is due in part to the quasi-flux limited nature of the parent sample and fact that the low-metallicity AGN tend to have low emission-line luminosities. The region in the diagram where metallicity is high and η is low is devoid of objects.

In order to simplify the process of calculating AGN oxygen abundances for pairs of $[O III]/H\beta$ and $[N II]/H\alpha$ ratios, we used singular value decomposition to fit the grid of flux-ratio predictions used to construct Figure 10 with a two-dimensional polynomial:

$$z = 7.863 + 1.170x + 0.027y - 0.369x^2 + 0.208y^2 - 0.406xy - 0.100x^3 + 0.323y^3 + 0.354x^2y - 0.333xy^2 \quad (25)$$

where $x = \log [N II]/H\alpha$, $y = \log [O III]/H\beta$, and $z =$

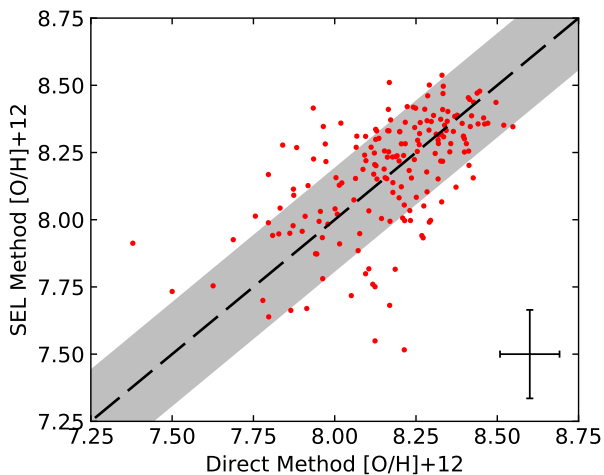


Figure 9. Comparison of $[\text{O}/\text{H}]+12$ values estimated from our SEL approach to those obtained via the direct method for the SDSS AGN sample. The width of the grey region, which includes 68% of the sample, indicates that application of the SEL method adds an uncertainty of 0.15 dex to the error in the direct method abundances of AGNs. The total 1σ error in the SEL abundances has a typical value of 0.18 dex.

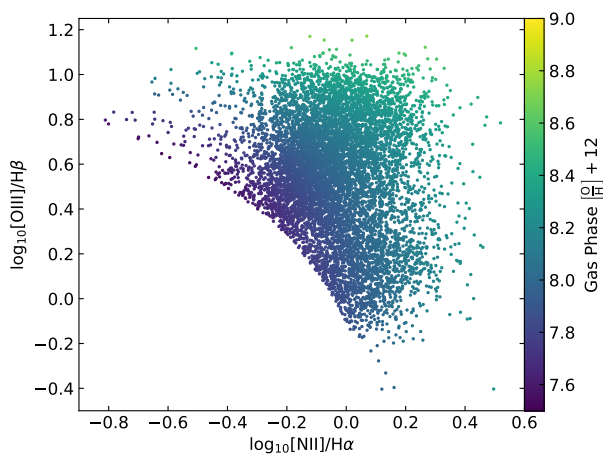


Figure 10. Oxygen abundances of the 8685 AGN in our SDSS parent sample, plotted according to their locations on the BPT diagnostic diagram.

$[\text{O}/\text{H}]+12$. In the $[\text{O}/\text{H}]+12 = 7.5 - 9.0$ range, abundances calculated from the polynomial fit are nearly indistinguishable from those derived via interpolation of the grid of predicted line ratios.

6.4 Implications for LINERs

The class of emission-line galaxies known as LINERs (Heckman 1980) occupy the lower portion of the AGN region on the $[\text{O III}]/\text{H}\beta$ vs. $[\text{N II}]/\text{H}\alpha$ BPT diagram. As Molina et al. (2018) discuss, a number of different processes can, and probably do, give rise to LINER-like emission lines in

galaxies. Strictly speaking, the AGN abundances predicted from our SEL method are valid only for objects that are powered by photoionization by a hard, non-stellar continuum associated with accretion onto a supermassive black hole. Unfortunately, it is generally not possible to identify the primary power source in LINERs from their optical spectra alone. Therefore, some caution is warranted when employing Equation 25 to estimate $[\text{O}/\text{H}]+12$ for objects that reside in the LINER region of the BPT diagram.

It has, however, been argued that the majority of LINERs are in fact bona fide AGN (Ho 2008). If this is true of LINERs in the SDSS parent sample, the SEL model outlined in § 6.1 lends insight into how these objects and classical Seyfert nuclei might be distinguished. Interpolating η over the flux ratios predicted for AGN from Equations 23 and 24 (as we did above for $[\text{O}/\text{H}]+12$), we find that the distribution of η values for the parent sample is bimodal, with peaks at $\eta = 0.107$ and $\eta = 0.312$ and a deep minimum at $\eta = 0.190$. This bimodality in η suggests that AGN in the parent sample belong to one of two distinct ionization groups: Seyferts ($\eta > 0.190$) or LINERs ($\eta < 0.190$). The two-dimensional histogram of line ratios shown in Figure 11 confirms that the parent sample AGN are concentrated into two well-separated groups on the BPT diagram. Furthermore, it is clear from the Figure that the curve associated with the SEL model for $\eta = 0.190$ provides a viable discriminator for Seyferts and LINERs. The curve can be approximated by the expression

$$y = \frac{-0.628}{x + 1.417} + 0.753 \quad (26)$$

where x and y are the base-ten logarithms of the $[\text{N II}]/\text{H}\alpha$ and $[\text{O III}]/\text{H}\beta$ flux ratios, respectively. Note that at the intersection with the Kewley et al. (2001) “maximum starburst” line, the $\eta = 0.190$ curve overlaps with the empirical Seyfert/LINER boundary proposed by Schawinski et al. (2007). But overall, the $\eta = 0.19$ curve appears to delineate the two classes of objects better, and it has the advantage of being physically tied to photoionization through the O^{+2} ion fraction, which gives rise to the $[\text{O III}] \lambda 5007$ emission line.

7 CONCLUSION

Metallicity estimates for AGN are necessary for a complete picture of the properties and evolution of the nuclear environments of galaxies. In this paper, we have derived measurements for the physical and chemical properties of SDSS AGN based on a simple three-zone ionization structure. From the inferred oxygen abundances and corresponding electron temperatures, we have obtained the first empirical cooling sequence and nitrogen production relations for Seyfert galaxies. Using the empirically-calibrated relations revealed by these results, we have reframed traditional emission-line flux-ratio diagnostic diagrams as probes of temperature and chemical composition in addition to ionization structure. Based on this insight, we have developed a method for estimating the direct-method abundances of AGN solely from the strong emission lines (SELS) commonly employed in BPT diagnostic diagrams. Our method can be expressed by a single equation as a function of observed

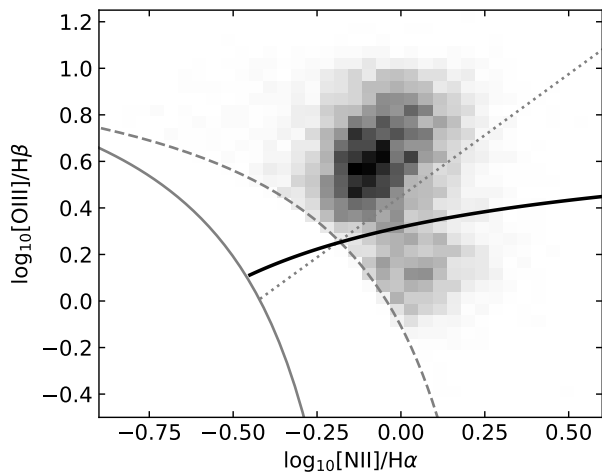


Figure 11. Distributions of AGN flux ratios for the SDSS parent sample. The darkest areas indicate where the densities of objects are greatest. Empirical (Kauffmann et al. 2003) and theoretical (Kewley et al. 2001) demarcations between H II galaxies and AGN are shown with solid and dashed grey curves, respectively. In the AGN zone, the empirical division between Seyfert galaxies and LINERs proposed by Schawinski et al. (2007) is indicated with a dotted line. The solid black curve, which represents the predictions of our SEL model for $\eta = 0.190$, appears to be more effective at discriminating between the two classes of objects.

SEL flux ratios, which is effective at recovering the direct-method abundances within the uncertainties of the measurements. We have applied our new method to ~ 8700 AGN with detected SELs in the SDSS DR8, which represents the largest sample of AGN with direct-method abundances to date. The use of SEL line ratios readily facilitates investigations into the evolution of chemical abundances in AGN. Although not our primary objective, our model also provides a viable, physically-motivated discriminator between Seyferts and LINERs.

Future work which might lead to refinements in this method include:

(i) Follow-up spectroscopy of AGN for which measurements of the [O II] doublet are lacking in order to extend the empirical relations to the local volume;

(ii) Estimates of the low-ionization temperature from the [N II] or [O II] auroral lines to obviate the electron temperature scaling employed in §3.2, followed by estimates of thermal inhomogeneities from computed temperatures to improve direct-method abundances;

(iii) More detailed comparisons between the results of our method and those found with object-specific photoionization models, general methods such as the Storchi-Bergmann et al. (1998) and Pérez-Montero et al. (2019) approaches, and SEL inference methods such as the traditional R_{23} diagnostic;

(iv) New photoionization modeling to confirm that the three-zone model is sufficient in recovering the total oxygen abundance.

While the results of this study prompt additional investigation, we have laid an important foundation for inferring the chemical abundances and ion fraction in AGN. Moreover,

the cooling sequence and nitrogen abundances in AGN have opened new opportunities for understanding chemical evolution and cooling processes in the ISM of galactic nuclei. Ultimately, chemical abundance estimates for large populations of AGN, combined with stellar population synthesis, will improve our understanding of the relationship between metallicity and star formation in AGN environments—insight that is essential for investigations of the AGN-starburst connection and the coevolution of AGN and their host galaxies.

REFERENCES

- Aihara H., et al., 2011, *ApJS*, **193**, 29
Aller L. H., 1942, *ApJ*, **95**, 52
Aller L. H., Liller W., 1959, *ApJ*, **130**, 45
Alloin D., Collin-Souffrin S., Joly M., Vigroux L., 1979, *A&A*, **78**, 200
Baldwin J. A., Phillips M. M., Terlevich R., 1981, *PASP*, **93**, 5
Burgess A., Seaton M. J., 1960, *MNRAS*, **121**, 76
Calzetti D., 2001, *PASP*, **113**, 1449
Cappellari M., Emsellem E., 2004, *PASP*, **116**, 138
Cruz-Gonzalez I., Guichard J., Serrano A., Carrasco L., 1991, *PASP*, **103**, 888
Diamond-Stanic A. M., Rieke G. H., 2012, *ApJ*, **746**, 168
Dors O. L., et al., 2013, *MNRAS*, **432**, 2512
Dors O. L., Cardaci M. V., Hägele G. F., Rodrigues I., Grebel E. K., Pilyugin L. S., Freitas-Lemes P., Krabbe A. C., 2015, *MNRAS*, **453**, 4102
Dors Jr. O. L., Arellano-Córdova K. Z., Cardaci M. V., Hägele G. F., 2017, *MNRAS*, **468**, L113
Esteban C., Bresolin F., Peimbert M., García-Rojas J., Peimbert A., Mesa-Delgado A., 2009, *ApJ*, **700**, 654
Evans I. N., Dopita M. A., 1987, *ApJ*, **319**, 662
Ferland G. J., et al., 2013, *Rev. Mex. Astron. Astrofis.*, **49**, 137
Ferland G. J., et al., 2017, *Rev. Mex. Astron. Astrofis.*, **53**, 385
Fernández-Ontiveros J. A., Spinoglio L., Pereira-Santaella M., Malkan M. A., Andreani P., Dasyra K. M., 2016, *ApJS*, **226**, 19
García-Bernete I., et al., 2016, *MNRAS*, **463**, 3531
Groves B. A., Dopita M. A., Sutherland R. S., 2004, *ApJS*, **153**, 9
Gutkin J., Charlot S., Bruzual G., 2016, *MNRAS*, **462**, 1757
Heckman T. M., 1980, *A&A*, **500**, 187
Ho L. C., 2008, *ARA&A*, **46**, 475
Izotov Y. I., Stasińska G., Meynet G., Guseva N. G., Thuan T. X., 2006, *A&A*, **448**, 955
Kauffmann G., et al., 2003, *MNRAS*, **346**, 1055
Kennicutt Jr. R. C., Bresolin F., Garnett D. R., 2003, *ApJ*, **591**, 801
Kewley L. J., Ellison S. L., 2008, *ApJ*, **681**, 1183
Kewley L. J., Dopita M. A., Sutherland R. S., Heisler C. A., Trevena J., 2001, *ApJ*, **556**, 121
Kewley L. J., Groves B., Kauffmann G., Heckman T., 2006, *MNRAS*, **372**, 961
Kewley L. J., Dopita M. A., Leitherer C., Davé R., Yuan T., Allen M., Groves B., Sutherland R., 2013, *ApJ*, **774**, 100
Kobulnicky H. A., Kennicutt Jr. R. C., Pizagno J. L., 1999, *ApJ*, **514**, 544
Koski A. T., 1978, *ApJ*, **223**, 56
Levesque E. M., Kewley L. J., Larson K. L., 2010, *AJ*, **139**, 712
López-Sánchez Á. R., Dopita M. A., Kewley L. J., Zahid H. J., Nicholls D. C., Scharwächter J., 2012, *MNRAS*, **426**, 2630
Luridiana V., Morisset C., Shaw R. A., 2015, *A&A*, **573**, A42
Maraston C., Strömbäck G., 2011, *MNRAS*, **418**, 2785
McGaugh S. S., 1991, *ApJ*, **380**, 140
Menzel D. H., Aller L. H., 1941, *ApJ*, **94**, 30

- Menzel D. H., Aller L. H., Hebb M. H., 1941, *ApJ*, **93**, 230
- Molina M., Eracleous M., Barth A. J., Maoz D., Runmoe J. C., Ho L. C., Shields J. C., Walsh J. L., 2018, *ApJ*, **864**, 90
- Nicholls D. C., Dopita M. A., Sutherland R. S., Jerjen H., Kewley L. J., Basurah H., 2014, *ApJ*, **786**, 155
- Nicholls D. C., Sutherland R. S., Dopita M. A., Kewley L. J., Groves B. A., 2017, *MNRAS*, **466**, 4403
- Oliva E., Marconi A., Cimatti A., di Serego Alighieri S., 1998, *A&A*, **329**, L21
- Osterbrock D., Ferland G., 2006, *Astrophysics of Gaseous Nebulae and Active Galactic Nuclei*. University Science Books
- Osterbrock D. E., Miller J. S., 1975, *ApJ*, **197**, 535
- Peimbert M., 1968, *ApJ*, **154**, 33
- Peimbert M., Costero R., 1969, Boletín de los Observatorios Tonantzintla y Tacubaya, **5**, 3
- Pérez-Montero E., Díaz A. I., 2003, *MNRAS*, **346**, 105
- Pérez-Montero E., Dors O. L., Vílchez J. M., García-Benito R., Cardaci M. V., Hägele G. F., 2019, arXiv e-prints, [p. arXiv:1908.04827](https://arxiv.org/abs/1908.04827)
- Pettini M., Pagel B. E. J., 2004, *MNRAS*, **348**, L59
- Pilyugin L. S., Grebel E. K., Mattsson L., 2012, *MNRAS*, **424**, 2316
- Rubin R. H., Colgan S. W. J., Haas M. R., Lord S. D., Simpson J. P., 1997, *ApJ*, **479**, 332
- Sarzi M., et al., 2006, *MNRAS*, **366**, 1151
- Schawinski K., Thomas D., Sarzi M., Maraston C., Kaviraj S., Joo S.-J., Yi S. K., Silk J., 2007, *MNRAS*, **382**, 1415
- Searle L., 1971, *ApJ*, **168**, 327
- Shuder J. M., Osterbrock D. E., 1981, *ApJ*, **250**, 55
- Spitzer Jr. L., 1949, *ApJ*, **109**, 337
- Stasińska G., Cid Fernandes R., Mateus A., Sodr e L., Asari N. V., 2006, *MNRAS*, **371**, 972
- Storchi-Bergmann T., Pastoriza M. G., 1990, *PASP*, **102**, 1359
- Storchi-Bergmann T., Schmitt H. R., Calzetti D., Kinney A. L., 1998, *AJ*, **115**, 909
- Str omgren B., 1939, *ApJ*, **89**, 526
- Sutherland R. S., Dopita M. A., 2017, *ApJS*, **229**, 34
- Sutherland R., Dopita M., Binette L., Groves B., 2013, MAP-PINGS III: Modelling And Prediction in Photoionized Nebulae and Gasdynamical Shocks, Astrophysics Source Code Library (ascl:1306.008)
- Talbot Raymond J. J., Arnett D. W., 1974, *ApJ*, **190**, 605
- Thomas D., et al., 2013, *MNRAS*, **431**, 1383
- Toribio San Cipriano L., Dom nguez-Guzm n G., Esteban C., Garc a-Rojas J., Mesa-Delgado A., Bresolin F., Rodr guez M., Sim n-D az S., 2017, *MNRAS*, **467**, 3759
- Veilleux S., Osterbrock D. E., 1987, *ApJS*, **63**, 295
- Vila-Costas M. B., Edmunds M. G., 1993, *MNRAS*, **265**, 199
- Vincenzo F., Belfiore F., Maiolino R., Matteucci F., Ventura P., 2016, *MNRAS*, **458**, 3466
- van Zee L., Salzer J. J., Haynes M. P., O'Donoghue A. A., Balonek T. J., 1998a, *AJ*, **116**, 2805
- van Zee L., Salzer J. J., Haynes M. P., 1998b, *ApJ*, **497**, L1

APPENDIX A: REDDENING CORRECTIONS

In the Portsmouth reduction pipeline, emission-line fluxes are corrected for extinction by applying the reddening inferred from their ssp template fit to the starlight continuum. In the majority of cases, however, this fails to account fully for the attenuation of the emission lines. Emission-line extinction corrections typically involve a comparison between observed and intrinsic values of the Balmer decrement $F_{H\alpha}/F_{H\beta}$. For an assumed reddening law $f(\lambda)$, the equation

of radiative transfer becomes

$$\frac{F_{H\alpha}}{F_{H\beta}} = \frac{F_{H\alpha,0}}{F_{H\beta,0}} 10^{-c[f(H\alpha)-f(H\beta)]} \quad (\text{A1})$$

where the subscript 0 denotes the intrinsic Balmer line fluxes and c is a scale factor related to the amount of extinction suffered by the observed radiation (OF06). However, the intrinsic Balmer decrement depends (albeit weakly) on electron temperature, so it is necessary to compute or assume an initial estimate of T_e in order to solve for c .

Ideally, the process should be iterative, following these steps: (i) estimate the electron temperature, (ii) determine the expected value of the intrinsic Balmer decrement given this estimate of T_e , (iii) solve for c (from which the color excess $E[B - V]$ can be derived), (iv) correct the emission-line fluxes for extinction and recompute T_e . We have explored this iterative technique by performing a Monte Carlo simulation based on 10^4 randomly generated observed Balmer decrements between 2.75 and 6, electron temperatures between 3,000 K and 30,000 K, and electron densities between 1 and 1,000 cm^{-3} . Values of the intrinsic Balmer decrement were computed using PYNEB to calculate the Case B emissivities for $H\alpha$ and $H\beta$. For estimating $E(B - V)$, we adopted the Calzetti (2001) extinction law.

The results of our simulation reveal a strong correlation between $E(B - V)$ and the observed Balmer decrement, which can be described as

$$E(B - V) = 1.943 \log_{10} \left(\frac{F_{H\alpha}}{F_{H\beta}} \right) - \left(0.81 + \frac{0.1}{0.266 + t_4} \right), \quad (\text{A2})$$

where $t_4 = T_e/10^4$ K. This expression is not strongly dependent on electron temperature, but overall its application yields better estimates of the intrinsic emission-line fluxes than those we would obtain assuming a single fixed value for the electron temperature.

This paper has been typeset from a $\text{\TeX}/\text{\LaTeX}$ file prepared by the author.